Kinetic Particle Simulation Study of Parallel Heat Transport in Scrape-off Layer Plasmas over a Wide Range of Collisionalities

Aaron FROESE, Tomonori TAKIZUKA[1)] and Masatoshi YAGI[2)]

IGSES, Kyushu University, Kasuga 816-8580, Japan
[1)]*Japan Atomic Energy Agency, Naka 311-0193, Japan*
[2)]*RIAM, Kyushu University, Kasuga 816-8580, Japan*

(Received 15 March 2010 / Accepted 10 June 2010)

Fluid models are not generally applicable to fusion edge plasmas without external provision of kinetic factors: closure parameters and boundary conditions inside the sheath region. We explain the PARASOL-1D simulation, a particle-in-cell code with a binary collision Monte-Carlo model, and use it to determine four kinetic factors commonly needed in fluid codes. These are the electron and ion heat flux limiting factors, α_e and α_i, the ion adiabatic index, γ_A, and the electron and ion temperature anisotropy, $T_\parallel/T_\perp$. We survey these factors over a wide range of collisionalities and find that, as predicted, the conductive heat flux is accurately described by the Spitzer-Härm expression in the collisional limit and asymptotes to a constant value in the collisionless limit. However, unique behavior occurs in the weakly collisional regime when the ratio of the mean free path to connection length is $0.1 < \lambda_{mfp}/L_\parallel < 10$, when the SOL is between the conduction- and sheath-limited regimes. We find that α_e can peak, becoming larger than the collisionless limit, γ_A is less than unity, and only the ions are anisotropic. The effects of electron energy radiation and Langevin heating are explored. Finally, the strong deviations of the energy distribution function from Maxwellian in the weakly collisional and collisionless regimes are explained.

Keywords: scrape-off layer, particle-in-cell simulation, heat flux limiting factor, adiabatic index

DOI: 10.1585/pfr.5.026

1. Introduction

In a tokamak, hot plasma is lost from the core by anomalous transport and edge localized modes (ELMs) and carried by parallel transport along the open field lines in the scrape-off layer (SOL) to the divertor plates. Parallel heat flux through the SOL in current generation tokamaks can be higher than 500 MWm^{-2} and ITER is expected to have double that amount [1]. To limit sputtering, which damages the divertor plates and causes impurities to enter the plasma, steady-state heat flux on the plate surface must remain less than 10 MWm^{-2}. Strategies presently used to reduce the heat load include inclining the divertor tiles, increasing magnetic flux expansion at the divertor, and increasing perpendicular transport in the SOL. The divertor geometry is also optimized to produce a detached divertor. The most appealing solution is to engineer the SOL behavior itself to increase the parallel temperature gradient. However, the empirical scaling of the heat flux to the divertor plates with respect to SOL properties has not yet been measured [2].

The SOL and plasma-surface interaction are highly complex features that must be modeled accurately in order to simulate realistic fusion devices. Since the SOL is a mediator between the hot core plasma and solid surfaces, the properties of the SOL plasma vary significantly along the magnetic field. Many 1d models have been developed to provide information about the density, temperature, flow velocity, and electric field along the magnetic field lines, which can be used to determine the energy out-fluxes to the divertor plate versus those to volumetric loss processes such as radiation.

In the collisionless regime, the plasma is isothermal, so the temperature can be specified as a parameter and the sheath can be ignored. Most early models use this technique and produce similar results. Tonks and Langmuir developed a kinetic model with cold ions in the 1920s to apply to low temperature, non-magnetic gas discharges in the collisionless and collisional limits [3]. More specific to the SOL, an isothermal fluid model with warm ions by Self and Ewald was presented in the 1960s [4]. Collisionless kinetic treatments have been developed by Emmert *et al.*[5] and Bissell and Johnson [6]. Additionally, two adiabatic, collisionless fluid models have been created by Bissell *et al.*[7] and Scheuer and Emmert [8]. The latter was also applied to a simple case in the collisional limit.

In the collisional SOL, one must specify the particle, momentum, and power inputs, as well as the nature of sources and sinks. This added complication essentially precludes the use of analytic models and many computer codes have been developed to solve this problem. Such

author's e-mail: aaron@riam.kyushu-u.ac.jp

codes include the fluid code EDGE1D [9] and the particle code PARASOL-1D [10]. The results of these 1d models can be thought of as providing profiles which are averaged over the width of the SOL. The cross-field transport and width of the SOL are not known, but must be taken from experiment and added as parameters.

Modern modeling efforts concentrate on 2d computer codes, which can self-consistently evaluate the cross-field particle and energy diffusion, as well as predict the radial profile of the SOL. A majority, such as B2 [11], UEDGE [12], EDGE2D [13], and SOLDOR [14] are fluid codes, which reduce the dimensionality by assuming a Maxwellian velocity distribution. However, the fluid model is not self-consistent; it requires closure parameters and boundary conditions inside the sheath region to be given by external models. These adjustments to the fluid model that reproduce kinetic effects must be supplied by analytic theory, experiment, or kinetic simulations, and hence are called kinetic factors (KF). Ideally, KF for 2d fluid codes should come from 2d experimental data or 2d kinetic simulations, both rare occurrences. Because of the large amount of computing power required to sample five dimensions, 2d3v fully kinetic codes are infrequently used. We are aware of only one particle-in-cell code, PARASOL-2D [15], and one Euler-Vlasov code [16] in existence. Gyrokinetic codes are more common and may produce adequate data for KF.

Since fluid codes are preferentially used in the treatment of edge plasmas, it is important that they implement kinetic effects with accurate models. In this work, we examine four KF: the electron and ion heat flux limiting factors, α_e and α_i, the ion adiabatic index, γ_A, and the electron and ion temperature anisotropy, $T_\parallel/T_\perp$, in a region of the SOL without sources or sinks. The heat flux limiting factors are used to accurately model the heat flux in the collisionless plasma. Rather than the ion fluid velocity, most experiments report the Mach number in the SOL. Therefore, the adiabatic index is necessary to determine the ion sound speed from the local temperature. Finally, fluid codes do not currently separate the temperatures parallel and perpendicular to the magnetic field, which typically differ by a factor of three [28]. Therefore, the temperature anisotropy must be known to adjust the calculated heat flux. We investigate the equilibrium response of these four KF to a range of collisionalities, recycling rates, and source models.

In the next section, fluid models and kinetic effect models that can be applied to them are briefly reviewed. Kinetic models, specifically that of the PARASOL-1D simulation, are explained in Sec. 3. Results from PARASOL-1D are presented and discussed in Sec. 4. Finally, the findings are summarized in Sec. 5.

2. Kinetic Effects in Fluid Models

2.1 Fluid model and closure

If we assume that the Coulomb collision mean free path (MFP) is much shorter than the connection length, $\lambda_{mfp} \ll L_\parallel$, then the plasma velocity distribution can be assumed to be Maxwellian so that only the macroscopic quantities of the plasma must be known. The fluid model, which relates the macroscopic properties to one another, is developed by taking the first few moments of the Boltzmann equation. This process is explained in all introductory plasma texts, e.g. [17], but we shall reproduce the equations here. Each plasma species is represented by the Boltzmann equation,

$$\frac{\partial f_\sigma}{\partial t} + \boldsymbol{v}\cdot\nabla_r f_\sigma + \frac{q_\sigma}{m_\sigma}(\boldsymbol{E}+\boldsymbol{v}\times\boldsymbol{B})\cdot\nabla_v f_\sigma = \boldsymbol{C}_\sigma + \boldsymbol{S}_\sigma \quad (1)$$

where $f_\sigma(\boldsymbol{r},\boldsymbol{v})$ is the phase-space distribution of species $\sigma \in \{e, i\}$, $\boldsymbol{v}$, q_σ and m_σ are the particle velocity, charge, and mass, $\boldsymbol{E}$ and $\boldsymbol{B}$ are the electric and magnetic fields, $\boldsymbol{C}_\sigma = \sum_j \boldsymbol{C}_{\sigma j}$ is the collision term between species σ and all other species j, and S_σ is the source term. If the collision and source terms are zero, the characteristics of the equation are

$$m_\sigma \frac{\mathrm{d}\boldsymbol{r}}{\mathrm{d}t} = \boldsymbol{v}, \qquad m_\sigma \frac{\mathrm{d}\boldsymbol{v}}{\mathrm{d}t} = q_\sigma(\boldsymbol{E}+\boldsymbol{v}\times\boldsymbol{B}), \quad (2)$$

where $\boldsymbol{r}$ is the spatial position of an individual particle. Each moment equation is obtained by multiplying Eq. 1 by a kernel function $z_n(\boldsymbol{v})$ and integrating over velocity space. The zeroth moment is found by multiplying by $z_0 = 1$ and integrating, giving the equation of continuity,

$$\frac{\partial n_\sigma}{\partial t} + \nabla\cdot(n_\sigma \boldsymbol{V}_\sigma) = \boldsymbol{S}^0_\sigma, \quad (3)$$

where n_σ is the species density, $\boldsymbol{V}_\sigma = \langle\boldsymbol{v}\rangle_\sigma$ is the fluid velocity with the brackets $\langle a\rangle_\sigma \equiv \int a f_\sigma(x,\boldsymbol{v})\mathrm{d}^3v / \int f_\sigma(x,\boldsymbol{v})\mathrm{d}^3v$ indicating an average of the property a over all velocity space, and $\boldsymbol{S}^n \equiv \int \boldsymbol{S} z_n(\boldsymbol{v})\mathrm{d}^3v$ is the nth moment of the source term. Since there are two unknowns, another equation is necessary. The first moment is found by multiplying by $z_1 = m_\sigma\boldsymbol{v}$ and integrating, giving the momentum balance equation,

$$m_\sigma\frac{\partial n_\sigma \boldsymbol{V}_\sigma}{\partial t} - n_\sigma q_\sigma[\boldsymbol{E}+\boldsymbol{V}_\sigma\times\boldsymbol{B}] + \nabla\cdot\boldsymbol{M}_\sigma = \boldsymbol{R}^1_\sigma + \boldsymbol{S}^1_\sigma, \quad (4)$$

where $\boldsymbol{M}_\sigma = n_\sigma m_\sigma(\boldsymbol{V}_\sigma\boldsymbol{V}_\sigma)$ is the momentum stress tensor, and $R^n_\sigma \equiv \int C z_n(\boldsymbol{v})\mathrm{d}^3v$ is the nth moment of the collisional friction. Since there are now three unknowns, yet another equation is necessary. The second moment is found by multiplying by $z_2 = (1/2)m_\sigma v^2$ and integrating, giving the energy balance equation,

$$\frac{1}{2}\frac{\partial}{\partial t}(\mathrm{Tr}M_\sigma) + \nabla\cdot\boldsymbol{Q}_\sigma - n_\sigma q_\sigma \boldsymbol{V}_\sigma\cdot\boldsymbol{E} = \boldsymbol{R}^2_\sigma + \boldsymbol{S}^2_\sigma, \quad (5)$$

where $\boldsymbol{Q}_\sigma \equiv (1/2)n_\sigma m_\sigma \left\langle v^2\boldsymbol{v}\right\rangle_\sigma$ is the energy flux. Each moment equation has one additional unknown that must be

determined from the next higher moment. The sequence is usually truncated here at the second or sometimes taken to the third moment. An external model is used to provide a value for the last unknown. For example, adiabatic fluid models assume that the heat flow is zero.

2.2 Kinetic factors

The fluid model reduces computation time, but eliminates details in velocity space, making it inaccurate when the energy distribution function (EDF) deviates from Maxwellian. Such deviation can occur when the MFP is long or there is an electric field, such as in the sheath region. Fluid codes are used when high spatial dimensionality is needed, but information regarding cross-field diffusion is more important than accurate modeling in the weakly collisional and collisionless regimes. Modern SOL fluid codes apply external models that attempt to correct for the loss of kinetic effects. These models are typically simple, relying on a single fitting parameter, which becomes a KF of interest. Kinetic factors include closure parameters that act volumetrically and boundary conditions at the sheath entrance, rather than the divertor plate.

The need for kinetic factors is nearly always due to a deviation of the plasma from a Maxwellian distribution. The parallel EDFs in the SOL are strongly affected by the collisionality. If the plasma is collisional, then there is strong diffusion in velocity space and the distribution is very close to Maxwellian. However, if the plasma is weakly collisional, simulations have shown that the electron distribution in the SOL has a low-energy symmetrical bulk population and a high-energy tail traveling towards the divertor plate [18, 19]. Because the bulk is almost symmetric, it will contribute very little to the fluid velocity or heat flux; most of the contribution will come from the high-energy tail. However, the tail properties cannot be determined from macroscopic quantities like the plasma density and temperature because the tail has a density much less than 1% of the bulk. Using an Eulerian code with Fokker-Planck collision operator, the bulk population was shown to have a double-lobed shape [20], which has not been reproduced with either PARASOL-1D [18] or BIT1 [19]. However, experimental results cannot resolve this conflict because they are not sensitive enough to differentiate the tail [21].

Regardless of collisionality, the plasma always deviates from Maxwellian in the Debye sheath, due to the strong electric field. The high-energy electrons are lost, while low-energy ones are reflected, creating a cut-off Maxwellian distribution. On the other hand, the ions are accelerated towards the divertor plate, causing a shifted-Maxwellian distribution [22]. Therefore, fluid models cannot model the sheath region self-consistently; the sheath region is ignored and all boundary conditions must be provided at the sheath entrance by an external model.

2.3 Closure parameters

The volumetric KF are the conductive heat flux, temperature anisotropy, and ion viscosity. Each of these can be calculated using the classical expression in the collisional limit [23], but require a functional dependence on collisionality to be useful in a fluid code. The ion and electron parallel energy fluxes can be divided into conductive heat flux, convective flux, viscous transport of energy, and convection of energy. The latter two are higher order components, so they can be neglected, leaving the definitions

$$Q_\sigma = \frac{n_\sigma m_\sigma}{2}\left\langle v_\parallel v^2\right\rangle_\sigma \approx q_\sigma^{\mathrm{cond}} + q_\sigma^{\mathrm{conv}}, \tag{6}$$

$$q_\sigma^{\mathrm{cond}} = \frac{n_\sigma m_\sigma}{2}\left\langle \tilde{v}_\parallel \tilde{v}^2\right\rangle_\sigma, \tag{7}$$

where $\tilde{\boldsymbol{v}} = \boldsymbol{v} - \boldsymbol{V}_\sigma$ is the random velocity of each particle. The convective and conductive components of the electron heat flux are roughly equal, but the ion heat flux is expected to be almost completely convective [24]. The conductive heat flux is approximated by the Spitzer-Härm expression [23, 25] in a collisional plasma,

$$\begin{aligned} q_\sigma^{\mathrm{SH}} &= -\kappa_\sigma^{\mathrm{SH}}\nabla_\parallel T_\sigma, \\ \kappa_{\mathrm{i}}^{\mathrm{SH}} &= 3.9 n_{\mathrm{i}} v_{\mathrm{ti}} \lambda_{\mathrm{ii}}, \\ \kappa_{\mathrm{e}}^{\mathrm{SH}} &= 3.2 n_{\mathrm{e}} v_{\mathrm{te}} \lambda_{\mathrm{ee}}, \end{aligned} \tag{8}$$

where $\kappa_\sigma^{\mathrm{SH}}$ is the heat conductivity, $T_\sigma = m_{\mathrm{e}}\left\langle v^2\right\rangle/3$ is the temperature, $v_{\mathrm{t}\sigma} = (T_\sigma/m_\sigma)^{1/2}$ is the thermal speed, $\lambda_{\sigma\sigma} = v_{\mathrm{t}\sigma}\tau_{\sigma\sigma}$ is the thermal MFP, and $\tau_{\sigma\sigma} \propto v_{\mathrm{t}\sigma}^3$ is the same-species collision time. This expression is valid when the actual heat flux is the less than the order of the Maxwellian one-way free-streaming heat flux

$$q_\sigma^{\mathrm{FS}} = n_\sigma T_\sigma \left(T_{\parallel,\sigma}/m_\sigma\right)^{1/2}, \tag{9}$$

where $T_{\parallel,\sigma} = m_{\mathrm{e}}\left\langle v_\parallel^2\right\rangle$ is the temperature parallel to the magnetic field. The collision-dependent heat flux is approximated by a harmonic average of Eqs. 8 and 9 [22],

$$q_\sigma^{\mathrm{eff}} = \left(\frac{1}{q_\sigma^{\mathrm{SH}}} + \frac{1}{\alpha_\sigma q_\sigma^{\mathrm{FS}}}\right)^{-1}, \tag{10}$$

where $\alpha_\sigma \equiv \lim_{\lambda_{\mathrm{mfp}}\to\infty} q_\sigma^{\mathrm{cond}}/q_\sigma^{\mathrm{FS}}$ is the flux-limiting coefficient, calculated as the ratio between the actual and one-way free-streaming heat flux in the collisionless limit.

In addition to heat flux limiting factors, the total heat flux is also affected by temperature anisotropy in the collisionless limit. Parallel energy is transported much faster than perpendicular energy, which causes the parallel temperature to decrease faster than the perpendicular energy. Fluid models assume a collisional plasma, which would eliminate any anisotropy, so the temperature anisotropy should be supplied to accurately calculate the heat flux.

Coulomb collisions act to transfer momentum when the colliding particles have similar mass. Ion-ion collisions give rise to ion viscosity and electron-electron collisions to electron viscosity. Since viscosity is diffusion of momen-

tum, the electron viscosity is smaller than the ion viscosity by a factor of the square root of the mass ratio, so it can be ignored. Similar to the heat flux, the parallel ion viscosity is often calculated as a limited harmonic average of the Braginskii ion viscosity,

$$\pi_{\|,\mathrm{i}} = \left(\frac{1}{\pi^{\mathrm{Br}}_{\|,\mathrm{i}}} + \frac{1}{b n_\mathrm{i} T_{\|,\mathrm{i}}} \right)^{-1}, \tag{11}$$

where

$$\pi^{\mathrm{Br}}_{\|,\mathrm{i}} = -(4/3)\eta_{\|,\mathrm{i}} \nabla_\| V_\|, \tag{12}$$
$$\eta_{\|,\mathrm{i}} = 0.96 n_\mathrm{i} T_\mathrm{i} \tau_\mathrm{i}$$

is the Braginskii viscosity and b is the ion viscosity limiting factor.

The heat flux limiting factors are usually assumed to be $\alpha_\sigma \approx 0.1$, although previous kinetic simulations have given values in the range $\alpha_\mathrm{i} = 0.1 \sim 2$ and $\alpha_\mathrm{e} = 0.03 \sim 3$ [24]. We have studied the heat transport in SOL plasmas with the PARASOL-1D code and shown that in a collisionless plasma where the ion-electron mass ratio is $m_\mathrm{i}/m_\mathrm{e} = 400$ and the plasma is in equilibrium, the electron heat flux limiting factor is $\alpha_\mathrm{e} = 0.75$ [26]. Further exploration showed that for a more realistic mass ratio of $m_\mathrm{i}/m_\mathrm{e} = 1800$, the value of α_e in a region of the SOL with no source or sink varies smoothly from a very small value when the electron radiation energy-loss rate is low to approximately unity when it is high [27].

The heat flux in the collisional and collisionless limits has been fully described by analytic theories [23, 25]. There has even been an attempt to explain the plasma behaviour in the weakly collisional regime [28]. However, even this approach must assume a Maxwellian distribution when providing fourth-order closure terms. Examination of the effect of collisionality using PARASOL-1D has shown that the heat flux does not follow a harmonic average transition from the collisional to the collisionless state, but peaks in the weakly collisional regime when the MFP is of the order of the system length and then decreases to the collisionless limit. The reason for the peak was found to be the development of a high-energy tail in the electron energy distribution as the plasma becomes collisionless [18, 19]. The tail effect is overpowered when electron radiation creates an asymmetry between the incoming and outgoing electron bulk distributions, thereby raising the heat flux in the collisionless limit and eliminating the peak.

While the harmonic average approximation is widely used (e.g. in B2-Eirene [29]), it has been found to be not generally valid [19, 30, 31, 34]. In kinetic particle-in-cell (PIC) simulations, the heat flux limiting factors and viscosity limiting factors vary by many orders of magnitude along the field line. The poloidal averages vary by an order of magnitude with collisionality [30] and also have a strong dependence on inelastic processes, such as recycling and radiation [19]. Using a fluid code, plasma profiles are found to be extremely sensitive to small changes in α_e [31], showing limiting factors to be poorly adapted for such application.

2.4 Boundary conditions

Boundary conditions must be provided at the sheath entrance, but the sheath is often highly dependent on properties integrated along the entire SOL. Therefore, we expect an accurate external model to be fairly complex. Simply measuring the properties at the sheath entrance is sufficiently difficult because the potential and electric field vary smoothly throughout the Debye sheath and magnetic presheath. The sheath entrance is not a clearly defined point, so we can define it using a number of conditions. For example:

1. A fixed point a specified number of Larmor radii from the wall is a good first-order estimate of the sheath entrance.
2. The point where the ion and electron charge densities become equal, $n_\mathrm{e} = Z_\mathrm{i} n_\mathrm{i}$, defines the sheath edge according to the quasineutral condition. The parameter Z_i is the charge per ion, which is one for a hydrogenic plasma.
3. The point where the ion and electron fluxes become equal, $n_\mathrm{e} V_{\|e} = Z_\mathrm{i} n_\mathrm{i} V_{\|\mathrm{i}}$, defines the sheath edge according to the ambipolar current condition.
4. The last point in front of the divertor where (under the driftless approximation) ions travel parallel to the magnetic field, $V_{x\mathrm{i}} = V_{\|\mathrm{i}} \sin\Theta$, defines the sheath edge according to the magnetized ion condition. The angle $\Theta = B_x/B$ is the ratio of the poloidal magnetic field to the total field strength and V_x is the flow velocity projected in the poloidal direction.
5. The point where the ion fluid velocity exceeds the sound speed $V_{\|\mathrm{i}} \geq c_\mathrm{s} = \sqrt{(T_{\|\mathrm{e}} + \gamma_\mathrm{A} T_{\|\mathrm{i}})/m_\mathrm{i}}$ defines the sheath edge according to the Bohm condition. The adiabatic index is defined as $\gamma_\mathrm{A} = 1 + (n/T_{\|\mathrm{i}})(\mathrm{d}T_{\|\mathrm{i}}/\mathrm{d}n_\mathrm{i})$. This differs from the common definition by using the parallel temperature instead of the isotropic temperature.

Using one or some combination of these definitions of the sheath entrance, the boundary conditions can be supplied as KFs. To accurately calculate energy-dependent sputtering rates, the ion heat transmission coefficient and velocity distribution function at the sheath entrance must be known. The heat transmission coefficient is defined as $\gamma_\sigma = Q_\sigma/\Gamma_\sigma T_\sigma$, where Γ_σ is the particle flux. The classical boundary conditions at the sheath are

$$\gamma_\mathrm{e} = 2 + \psi, \tag{13}$$
$$\gamma_\mathrm{i} = 2.5 + 0.5(\gamma_\mathrm{A} + T_\mathrm{e}/T_\mathrm{i}) + \Delta\gamma_\mathrm{i}, \tag{14}$$
$$M \equiv V_{\|,\mathrm{i}}/c_\mathrm{s} \approx 1, \tag{15}$$
$$\psi \equiv e\phi_\mathrm{SE}/T_\mathrm{e} \approx 0.5 \ln m_\mathrm{i}/m_\mathrm{e} \sim 3, \tag{16}$$

Table 1 Summary of kinetic factors that can be applied to fluid codes.

kinetic factor		used	range
elec. heat flux limit. factor	α_e	0.1	0.03-3
ion heat flux limit. factor	α_i	0.1	0.1-2
ion viscosity limit. factor	b	0.5	
Mach number	M	1	
adiabatic index	γ_A	2	1-3
heat transmis. coeff.	γ_e		4.5-5.5
heat transmis. coeff.	γ_i		2-3
norm. sheath potential	ψ	3	

where $|\Delta\gamma_i| < 1$ is a kinetic correction to the ion heat transmission coefficient [30], M is the Mach number, and ϕ_{SE} is the potential at the entrance to the magnetic presheath, which includes the potential drop across both the Debye sheath and magnetic presheath.

2.5 Summary of kinetic factors

The KF of interest are the heat flux limiting factors α_σ, the ion viscosity limiting factor b, the Mach number M or the adiabatic index γ_A, the temperature anisotropy $T_{\|,\sigma}/T_{\perp,\sigma}$, the heat transmission coefficients γ_σ, and the normalized sheath potential, ψ. The ion viscosity limiting factor $b \approx 0.5$ is usually used, but it has been found in the range $0.1 \sim 0.5$ [30]. According to the Bohm condition, the Mach number should be at least unity at the sheath edge. The heat transmission coefficients should fall within the range $\gamma_i = 2 \sim 3$ and $\gamma_e = 4.5 \sim 5.5$ as given by [22], although experiments show that this range is too restricted [32]. Since the plasma is magnetized, it has two degrees of freedom, and therefore the adiabatic index should be approximately 2. The expected range of each KF is summarized in Table 1.

3. Particle Simulation

3.1 Kinetic models

Kinetic models do not suffer from the shortcomings of fluid models because they simulate the full 3d-position and 3d-velocity space, but require much more computational power. Hence, they can be used to supply KF models for the faster fluid codes. There are three common fully kinetic computational methods for evaluating the evolution of the plasma: Eulerian mesh, semi-Lagrangian mesh, and particle simulations. The mesh techniques, described in introductory computational fluid mechanics texts, evaluate the Boltzmann equation (Eq. 1) to determine the plasma distribution over phase-space. The Eulerian mesh algorithm computes the plasma flow on a rigid grid of points in phase-space using, for example, finite difference or spectral equations. In contrast, the semi-Lagrangian mesh algorithm starts each step with a regular layout of fluid elements and allows each point to evolve freely according to the Lorentz force, then interpolating back to a regular layout to begin the next step. This is typically accomplished with the predictor-corrector method.

Mesh algorithms are highly accurate, but they experience numerical dissipation and restrictive stability conditions. Atomic/molecular processes and the plasma-wall interaction are also notoriously difficult to model [33]. For example, the collisions in the Boltzmann equation are described by the Fokker-Planck model [17]. However, such a collision operator requires order N^2 computation, where N is the total number of particles or grid points tracked in the simulation. Therefore, the Fokker-Planck model is often replaced with a simplification or with the Krook collision term [17]. The Krook model assumes a normally distributed background of neutral particles which elastically collide with the charged particles. Since the solution of the Boltzmann equation is a phase-space distribution function, it must be sufficiently sampled over 1+3+3 dimensions (time, 3 spatial, and 3 velocity), which is difficult for current computing systems. By assuming symmetries, such as homogeneity in the toroidal direction or perpendicular to the magnetic field, the dimensionality can be reduced to 1+2+3 or 1+2+2 dimensions, respectively. By tracking the electrons by their gyro-averaged trajectories, the minimum time-step can be increased and the velocity dimension of the electron fluid can be reduced by one.

Particle simulations are more representative of the physical reality. Instead of using the Boltzmann equation, a collection of particles is evolved according to the Lorentz force characteristics (Eq. 2). Fields and Lorentz forces are interpolated from the charge distribution tabulated on a separate spatial grid. Particle properties are usually updated using the leapfrog algorithm, which is described in Eq. 21. In contrast to mesh-only methods, it is relatively simple to implement collisional processes using the PIC algorithm, but this method suffers from high stochastic noise. A pair of classic texts [35, 36] describe the fundamentals of the PIC algorithm, while newer developments are covered in a recent review article [37].

3.2 Geometry and boundary conditions

The PARASOL-1D code employs a self-consistent electrostatic particle-in-cell model with a binary collision model [10, 26]. A slab geometry is used, such that motion is restricted to the direction parallel to the magnetic field and perpendicular gradients are zero, $\nabla_\perp = 0$. Results from PARASOL-1D represent a radial average over the region outside the separatrix. Position along the magnetic field line with connection length $L_\|$ is given by coordinate s and position in the poloidal direction with circumference L is given by coordinate x, as labeled in Fig. 1. The poloidal and parallel directions are related by the magnetic field angle of incidence on the divertor plate, $x = \Theta s$ and $L = \Theta L_\|$. Ion velocities in the poloidal, radial, and toroidal

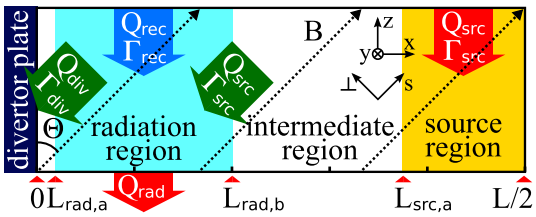

Fig. 1 Half of simulation domain showing source/sink regions, magnetic field, and flux parameters. Sources are displayed as arrows coming from the top and sinks as arrows leaving the bottom. Parallel fluxes are shown crossing boundary lines. src=hot source, rec=recycling, rad=radiation, div=divertor, x=poloidal axis, s=axis parallel to B, Γ=particle flux, Q=heat flux.

directions are denoted as v_x, v_y, and v_z, respectively. The spatial domain is symmetric across the midpoint, with divertor plates located at $x = 0$ and $x = L$. There is no difference between inboard and outboard divertor plates to avoid masking the physics we wish to observe. The domain is divided into three major regions: source, intermediate, and radiation/recycling. The range of the source region is $x = [L_{\mathrm{src},a} : L/2] = [0.4L : 0.5L]$, the radiation/recycling region is $x = [L_{\mathrm{rad},a} : L_{\mathrm{rad},b}] = [0.01L : 0.21L]$, and the intermediate region lies between them.

For this study, the number of spatial cells is set to 800 and the number of ions to $N_0 = 10^6$, which provides over 1000 particles-per-cell. In general, the time step must be much less than the inverse of collision frequency, $\nu\Delta t \ll 1$, for the collision algorithm to be accurate. The time step is set to the inverse plasma frequency, $\Delta t = \omega_{\mathrm{pe}}^{-1}$, which is valid for all but the most collisional plasmas. A smaller time step, $\omega_{\mathrm{pe}}\Delta t < 1$, would be required to satisfy $\nu\Delta t \ll 1$ when $\lambda_{\mathrm{mfp}}/L_{\parallel} < 10^{-3}$. The simulation is performed until a stationary state is achieved, which requires approximately

$$K_{\mathrm{eq}} = \frac{2L}{c_{\mathrm{s}}\Delta t} \approx 2\frac{L}{\lambda_{\mathrm{D}}}\sqrt{\frac{m_{\mathrm{i}}}{m_{\mathrm{e}}}} \tag{17}$$

steps, where $\lambda_{\mathrm{D}} \equiv (\varepsilon_0 T_\sigma/n_\sigma e_\sigma^2)^{1/2}$ is the Debye length. Equilibrium is confirmed by a visual examination of the density and temperature profiles; we ensure that the average change of each profile in 2000 time steps is less than the stochastic error of about 1%. In this case, equilibrium is estimated to occur by $K_{\mathrm{eq}} \sim 10^5$, which takes approximately 6 hours on 12 modern CPUs running in parallel. Equilibrium data is acquired by averaging over time between 1.8×10^5 steps and 2.0×10^5 steps.

3.3 Numerical scheme

The order of operations in PARASOL-1D is shown in Fig. 2. The initial condition of each run is a stationary plasma with uniform temperature, and density $n_0 \equiv \varepsilon_0 m_{\mathrm{e}}/e^2$. At the start of each step the particles are sorted by mesh cell but otherwise randomized, so that adjacent addresses in memory contain particles that occupy the same

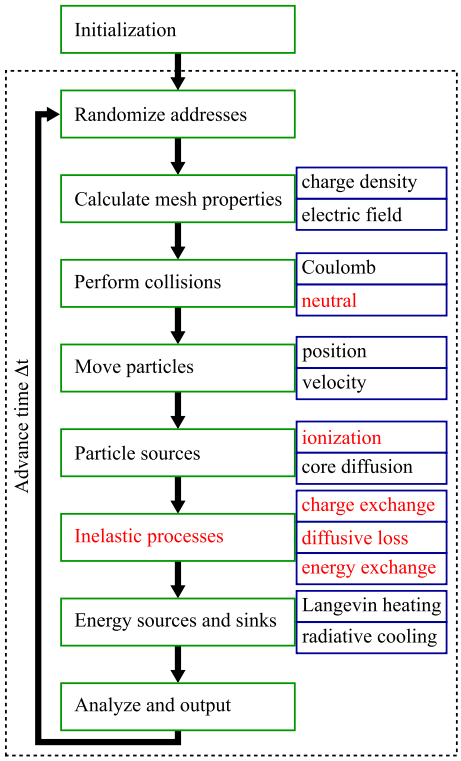

Fig. 2 Order of operations in PARASOL-1D code. Particle and energy souces are also inelastic processes, but are grouped separately to show their motivation. Modules that were active in the generation of results in this paper are black, while inactive ones are red.

cell, simplifying the following Coulomb collision procedure. The charges are projected to the mesh using the particle-in-cell procedure with a linear-weighting shape factor, as described by [35], with width equal to the cell size Δx,

$$S(x, x_i) = \begin{cases} \frac{1}{2\Delta x}\left(1 - \frac{|x-x_i|}{\Delta x}\right) & \text{if } |x - x_i| < \Delta x \\ 0 & \text{if } |x - x_i| > \Delta x, \end{cases} \tag{18}$$

such that each mesh point acquires a charge of

$$n_\sigma(x_j) = \sum_i q_\sigma \int \mathrm{d}x S(x_i - x_j), \tag{19}$$

where x_i is the position of particle i and x_j is the position of mesh point j. The potential is calculated from the density using Poisson's equation

$$-\nabla^2\phi = (e/\varepsilon_0)(Z_{\mathrm{i}}n_{\mathrm{i}} - n_{\mathrm{e}}), \tag{20}$$

using the tri-diagonal matrix algorithm on the equivalent second-order finite difference equation. It is then straightforward to find the electric field at the location of each particle, using the same shape factor as Eq. 19.

The ions are fully traced (1d3v), electrons follow their guiding centers (1d2v), and neutrals follow straight trajectories. There is a single species of ion with trajectories calculated by Eq. 2 in fields $\boldsymbol{E} = E_x\hat{x} + E_y\hat{y}$ and

$\boldsymbol{B} = \Theta B\hat{x}+(1-\Theta^2)^{1/2}B\hat{z}$, where E_x is the poloidal field normal to the divertor plates that is determined by the plasma potential and E_y specifies the strength of the $E \times B$ drift. The amplitude of the magnetic field B is specified by the ion gyro-radius normalized to the poloidal circumference ρ_i/L.

The positions and velocities of the ions are updated using the leapfrog algorithm and the electrons are updated using the predictor-corrector method. The leapfrog method used to advance the ions in time calculates positions at integer steps and velocities at half-steps,

$$\begin{aligned} &m_\mathrm{i}\left(\boldsymbol{v}^{\Delta t/2}-\boldsymbol{v}^{-\Delta t/2}\right)/\Delta t = \\ &\quad q_\mathrm{i}\left[\boldsymbol{E}(\boldsymbol{r}^0)+\left(\boldsymbol{v}^{\Delta t/2}+\boldsymbol{v}^{-\Delta t/2}\right)\times\ \boldsymbol{B}(\boldsymbol{r}^0)\right], \\ &\left(\boldsymbol{r}^{\Delta t}-\boldsymbol{r}^0\right)/\Delta t = \boldsymbol{v}^{\Delta t/2}, \end{aligned} \tag{21}$$

where the superscripts denote the time step relative to the previously calculated step. The equations that guide the electron gyrocenters are

$$\frac{\mathrm{d}\boldsymbol{r}}{\mathrm{d}t} = v_\parallel\frac{\boldsymbol{B}}{B}+\boldsymbol{v}_{E\times B}+\boldsymbol{v}_{\nabla B}, \tag{22}$$

$$m_\mathrm{e}\frac{\mathrm{d}v_\parallel}{\mathrm{d}t} = -e\frac{\boldsymbol{E}\cdot\boldsymbol{B}}{B}-\mu\nabla_\parallel B+m_\mathrm{e}v_\parallel\boldsymbol{v}_{E\times B}\cdot\frac{\nabla B}{B}, \tag{23}$$

where $v_\parallel$ is the velocity parallel to the magnetic field, $\boldsymbol{v}_{E\times B}$ is the $E\times B$ drift, $\boldsymbol{v}_{\nabla B}$ is the curvature drift, and $\mu \equiv mv_\perp^2/2B$ is the magnetic moment. The predictor-corrector method first calculates the values half a time step ahead using an explicit scheme. Then the correction step solves the equations $m_\mathrm{e}(v_\parallel^{\Delta t}-v_\parallel^0)/\Delta t = F_\parallel^{\Delta t/2}$ and $(\boldsymbol{r}^{\Delta t}-\boldsymbol{r}^0)/\Delta t = \boldsymbol{v}^{\Delta t/2}$ using the predicted half-step values. Any particles that reach the divertor plate are removed from the system.

3.4 Collision model

Coulomb collisions are simulated using a binary collision model that accurately models the Landau collision integral [38]. The collision time is equal for all particles. In each time step, each particle collides with an electron and an ion that occupy the same cell. The algorithm ignores separation of the particles at length scales smaller than the cell size. Due to the sorting already performed, it is efficient to pair adjacent addresses for same-species collisions and corresponding addresses for electron-ion collisions. Where the electron and ion number differ in a cell, members of the smaller population may undergo the collision procedure multiple times to ensure that all the members of the larger population undergo at least one collision procedure. Each collision conserves total energy and momentum. The deflection angle θ from the relative velocity $\boldsymbol{u}$ in the center of mass system of a particle of species α due to species β is

$$\tan\frac{\theta_\alpha}{2} \equiv \left(\frac{n_\alpha Z_\alpha^2 Z_\beta^2 e^4\ln\Lambda}{8\pi\varepsilon_0^2 m_{\alpha\beta}^2 u^3}\frac{\Delta t}{N_\mathrm{c}}\right)^{1/2}, \tag{24}$$

where ε_0 is the permittivity of free space, N_c is the number of times the collision algorithm is performed on a particle in a time step of length Δt, e is the elementary charge, $\ln\Lambda$ is the Coulomb logarithm, and $m_{\alpha\beta} \equiv m_\alpha m_\beta/(m_\alpha+m_\beta)$ is the reduced mass. The azimuthal angle of the deflection relative to $\boldsymbol{u}$ is random. By contrast, neutral collisions use a Monte Carlo model to simulate charge-exchange collisions, which are deactivated in the data presented.

The initial MFP is specified as an input parameter that is related to physical parameters as

$$\lambda_\mathrm{mfp0} \equiv 3^{3/2}\lambda_\mathrm{ee} = \frac{6\sqrt{3}\pi\varepsilon_0^2}{e^4 n_\mathrm{e0}\Lambda}T_\mathrm{e0}^2, \tag{25}$$

where the subscript '0' indicates an initial value. The actual MFP evolves with the local plasma density and temperature such that $\lambda_\mathrm{mfp}/\lambda_\mathrm{mfp0} = n_\mathrm{e0}/n_\mathrm{e}(T_{e\parallel}/T_\mathrm{e0})^{1/2}(T_\mathrm{e}/T_\mathrm{e0})^{3/2}$. Characteristics of the SOL plasma are determined mainly by collisionality and the quasineutral condition, except in the sheath region. In order to ensure the collisionless sheath condition in the present study, we adopt a collision cut-off at a distance $0.01L$ from the divertor plate, inside which the collision operation is not performed.

3.5 Source and sink models

Particle sources consist of the hot particle source region and recycling region, while sinks include the divertor plates and cross-field particle diffusion. Ions lost to the 100% absorptive divertor plates are replaced one-to-one at the hot particle and cold recycling sources, $\Gamma_\mathrm{div,i} = \Gamma_\mathrm{src,i}+\Gamma_\mathrm{rec,i}$, except when simulating ELMs. Particle generation is ambipolar, so electron and ion source fluxes are equal, $\Gamma_\mathrm{src,e} = \Gamma_\mathrm{src,i}$, $\Gamma_\mathrm{rec,e} = \Gamma_\mathrm{rec,i}$. Because the ion number is maintained, but the electrons escape quickly to the divertor, a sheath potential forms and a positive bias develops in the plasma. The ratio of recycling to hot source particle generation is an input parameter $R = \Gamma_{\mathrm{rec},\sigma}/(\Gamma_{\mathrm{src},\sigma}+\Gamma_{\mathrm{rec},\sigma})$. Hot electrons and ions are generated uniformly in space within the source region with isotropic thermal distributions of temperature T_e0 and T_i0, respectively. Cold particles are generated uniformly within the radiation/recycling region with isotropic thermal distributions of temperature $T_\mathrm{rec,e}$ and $T_\mathrm{rec,i}$. ELM pulses can be injected into the hot source region and cross-field particle diffusion is implemented as a probabilistic loss of ion-electron pairs that is unrestricted by region. Neither of these procedures have been applied in this investigation.

Energy sources and sinks consist of Langevin heating in the source region, electron radiative cooling in the radiation/recycling region, cross-field energy diffusion, and interaction with neutrals. When the Langevin heat bath model is activated, each particle j lying within the source region experiences heating given by the Langevin equation,

$$\frac{\Delta\boldsymbol{v}_j}{\Delta t} = -\nu\boldsymbol{v}_j+A, \qquad \left\langle A^2\right\rangle = 2\frac{T_{L0}}{m_j}\frac{\nu}{\Delta t}, \tag{26}$$

where ν is the Langevin relaxation constant, A is a ran-

dom variable with uniform distribution in the range set by the given temperature T_{L0}, and m_j is the particle mass. This heating model alters the speed of the particles, but not their direction of travel. The relaxation rate must be much smaller than unity, so that the speed of each particle does not change significantly in one step. Since all particles are affected, this model ensures that the velocity distribution tends towards Maxwellian even in a collisionless plasma with poor mixing.

Similarly, the electron radiative cooling model is implemented by decelerating all electrons in the radiation/recycling region while leaving their direction of travel unchanged. Each electron loses a fraction of the incoming energy flux proportional to its own kinetic energy. The relative change in kinetic energy in a period Δt is equal for each electron j and is much smaller than unity,

$$m_j \frac{\Delta v_j^2}{\Delta t} = -\frac{v_j^2}{\sum_k v_k^2} f_{\text{rad}} Q_{\text{src}}, \tag{27}$$

where the ratio of the desired radiation energy-loss flux to the energy flux from the source is given as an input parameter $f_{\text{rad}} = Q_{\text{rad}}/Q_{\text{src}}$ and the sum is performed over each electron k in the radiation/recycling region. Cross-field energy exchange employs the same algorithm as electron radiation to remove particle kinetic energy, but it can occur over the entire connection length. Neutral particles can be modeled via Monte-Carlo ionization and charge exchange reactions, but are ignored in the present study. Neither energy exchange nor neutral reactions are used in this study.

3.6 Estimation of measurement error

Finally, the last step in each cycle is to analyze the kinetic properties of the plasma. Output consists of three types of run-time analysis: temporal profiles, spatial profiles, and velocity distribution histograms. Temporal profiles are produced by directly reporting the plasma properties in a single cell at each time step, $\Delta K = 1$. No spatial averaging is performed, so the width of the averaging region relative the poloidal circumference is the width of a single mesh point, $\Delta l/L = 1/800$. The error in the temporal data is on the order of

$$\delta = 1/\sqrt{\Delta K N (\Delta l/L)} \approx 3\%. \tag{28}$$

Spatial profiles are produced by averaging the plasma properties over $\Delta K = 2000$ time steps to produce smooth results. Therefore, the error in the spatial distribution is only

$$\delta = 1/\sqrt{\Delta K N (\Delta l/L)} \approx 0.1\%, \tag{29}$$

where N is the number of particles tracked in the simulation.

To create the velocity distribution histograms, the domain length is divided into sections of width $\Delta l/L = 1/11$. All particles in each section are binned by velocity over a time period of $\Delta K = 2000$ steps. For this study, we report results from the section that is contained entirely within the intermediate region, $s/L_{\|} = [0.27 : 0.36]$. The parallel velocity is divided into $n_{\|,\text{bin}} = 100$ bins and the perpendicular into $n_{\perp,\text{bin}} = 50$ bins. The size of each bin is a small fraction of the thermal velocity, $\Delta v = 0.1 v_{T0}$. In this paper, we present the velocity distributions averaged over the perpendicular directions. Assuming uniform distribution in velocity space, each bin has order 10^3 particles, so the average error is

$$\delta = 1/\sqrt{\Delta K (N/n_{\|,\text{bin}})(\Delta l/L)} \approx 0.1\%, \tag{30}$$

which is a reasonable estimate at the distribution peak. It is more accurate to assume a Maxwellian distribution. The maximum velocity at which the error becomes equal to the signal amplitude, $\delta \sim 1$, is found by evaluating

$$1 = \Delta K \left(\frac{\Delta l}{L}\right) N \frac{\Delta v}{v_{T0}} \exp\left(\frac{-v_{\text{err}}^2}{v_{T0}^2}\right), \tag{31}$$

which gives the maximum velocity $v_{\text{err}} \approx 4.0 v_{T0}$, corresponding to a drop from maximum of about 10^{-7}. However, when examining the distribution functions in the results section, it appears that the data is overcome by noise at a lower value of $v_{\text{err}} \approx 3.0 v_{T0}$, corresponding to a drop from maximum of about 10^{-4}. This is consistent with a local density that is one order of magnitude less than the average, which can occur when the radiation is high or Langevin heating is used.

3.7 Measurement and noise reduction

Some post-processing is necessary to measure a number of plasma properties, namely the flux asymmetry, the spatial gradients, and the location of the sheath entrance. Before any calculations are done, all spatial profiles are smoothed by replacing each point j with an average of the five nearest points, $a_j = (a_{j-2} + a_{j-1} + a_j + a_{j+1} + a_{j+2})/5$, where appropriate adjustments are made at the edges of the domain. To determine the flux asymmetry of the distribution, the velocity distribution of the population traveling away from the divertor plate is subtracted from that of the population traveling towards it,

$$\Xi\{f_\sigma(v_\|)\} = f_\sigma(\tilde{v}_\|) - f_\sigma(-\tilde{v}_\|). \tag{32}$$

Likewise, the heat flux asymmetry can be obtained as

$$\Xi\{\tilde{v}_\|^3 f_\sigma(v_\|)\} = \tilde{v}_\|^3 \left[f_\sigma(\tilde{v}_\|) - f_\sigma(-\tilde{v}_\|)\right], \tag{33}$$

where $\tilde{v}_\| = v_\| - V_{\|,\sigma}$ is the velocity relative to the fluid velocity. The spatial gradients are obtained by the second-order finite difference definition $a'_j = (a_{j+1} - a_{j-1})/2h$, where h is the cell width. Unfortunately, even when using smoothed input data, this process adds a significant amount of noise. To acquire useful results, a 21-point average is performed, which reduces the noise to managable levels.

To find the sheath entrance, we use the average location at which sheath conditions 1-4 described in Sec. 2.4

are fulfilled. Each cell from the edge of the source region to the divertor plate is checked until the following inequalities are no longer satisfied,

$$1. \quad x \approx 3\rho_L, \tag{34}$$

$$2. \quad |Z_i n_i - n_e| < \epsilon(n_e + Z_i n_i)/2, \tag{35}$$

$$3. \quad |Z_i n_i V_i - n_e V_e| < \epsilon(n_e V_e + Z_i n_i V_i)/2, \tag{36}$$

$$4. \quad \left|V_{\|i}\Theta - V_{xi}\right| < \epsilon(V_{\|i}\Theta + V_{xi})/2, \tag{37}$$

where ϵ is a small non-zero adjustable parameter required to compensate for PIC noise. We find 0.03 to give good results.

4. Results and Discussion

The results presented in this section are for simulations of a hydrogenic plasma, $Z = 1$ and $m_i/m_e = 1800$, with equal electron and ion source temperatures, $T_{e0} = T_{i0}$. The magnetic field angle of incidence is $\Theta = 0.2$ and the ion gyro-radius is $\rho_i/L = 5 \times 10^{-3}$. There is no recycling from the divertor plates and no neutral collisions. Figure 3 shows the ratio of the electron conductive heat flux to the Spitzer-Härm collisional approximation and to the one-way free-streaming heat flux of a Maxwellian distribution with the same flow velocity and temperature. Figure 3 (a) clearly shows that the Spitzer-Härm expression (Eq. 8) is accurate when the MFP is less than the connection length, $\lambda_{mfp} < L_{\|}$. Figure 3 (b) indicates that the electron conductive heat flux does approach some constant fraction of the one-way free-streaming heat flux (Eq. 9), but only after a gradual decline from a peak at $\lambda_{mfp} \sim L_{\|}$ when the radiation rate is low. These plots show that the justification for using a harmonic average of the two limits is reasonable, but the presence of the peak in Fig. 3 (b) is difficult to accommodate using such a simple theory. High radiation rates create a strong temperature gradient and low plasma densities in the intermediate region. This reduces the MFP, pushing all the data points for the high radiation case to the left in the figures.

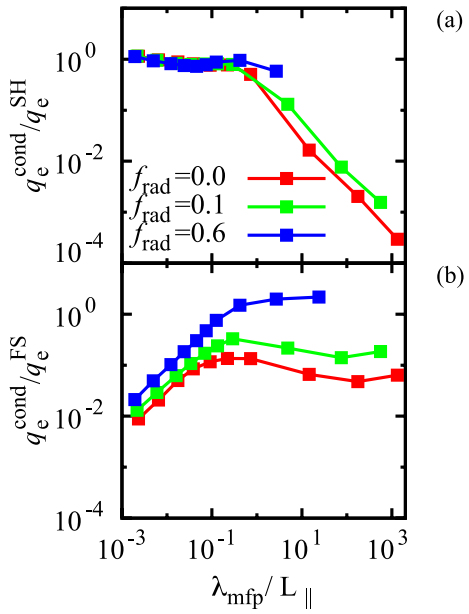

Fig. 3 Dependence on normalized MFP of ratio of electron conductive heat flux to (a) the Spitzer-Härm collisional approximation (Eq. 8), and to (b) the one-way free-streaming heat flux of a Maxwellian distribution with the same flow velocity and temperature (Eq. 9) for three different radiation rates. All values measured at equilibrium in range $s/L_{\|} = [0.27 : 0.36]$ with only hot particle source present.

4.1 Radiation effects on kinetic factors

The four KF of interest, the electron and ion heat flux limiting factors, adiabatic index, and parallel/perpendicular temperature anisotropy, are shown in Fig. 4 as a function of the normalized MFP, $\lambda_{mfp}/L_{\|}$, and radiation rate, f_{rad}. Corresponding plasma properties for the high and low radiation cases are shown in Fig. 5. These include the ion density and its gradient, Mach number and its gradient, ion parallel temperature and its gradient, plasma potential, and electric field. All values are acquired at equilibrium in the intermediate region with only the hot particle source present. By observing these figures, it is apparent that the plasma has significantly different behavior in the three regimes: collisional $\lambda_{mfp}/L_{\|} < 10^{-2}$, weakly collisional $10^{-2} < \lambda_{mfp}/L_{\|} < 1$, and collisionless $1 < \lambda_{mfp}/L_{\|}$. The collisional and collisionless limits can be solved analytically, but the response of the KF in the weakly collisional regime has not yet been adequately explained.

Figures 4 (a) and (b) show the electron and ion heat flux limiting factors, α_e and α_i, respectively. Since the heat flux approaches the Spitzer-Härm expression in the collisional limit, the heat flux limiting factors decrease proportional to the MFP as the contribution from the one-way free-streaming component to the harmonic average becomes negligible. In the collisionless limit, both the heat flux limiting factors appear to become constant when $\lambda_{mfp}/L_{\|} \sim 1$. In the absence of radiation, the limiting factors approach $\alpha_e \to 0.04$ and $\alpha_i \to 0.4$. When the radiation rate is high, $f_{rad} = 0.6$, the electron limiting factor increases by an order of magnitude, $\alpha_e \to 1$, but α_i does not change. High radiation produces a perpetual fluctuation in the collisionless regime which prevents true equilibrium from being attained.

The adiabatic index shown in Fig. 4 (c) is greater than unity in the collisional and collisionless regimes, but it dips to $\gamma_A = 0.5$ in the weakly collisional regime. High radiation causes the drop to less than unity to shift to much longer MFP; from $\lambda_{mfp}/L_{\|} = 0.03$ to 3. Typically the adiabatic index is calculated using the isotropic temperature, making values less than unity impossible. By calculating with the parallel temperature, it becomes a good indicator of transport. A value less than unity means that the density and temperature gradients point in opposite direc-

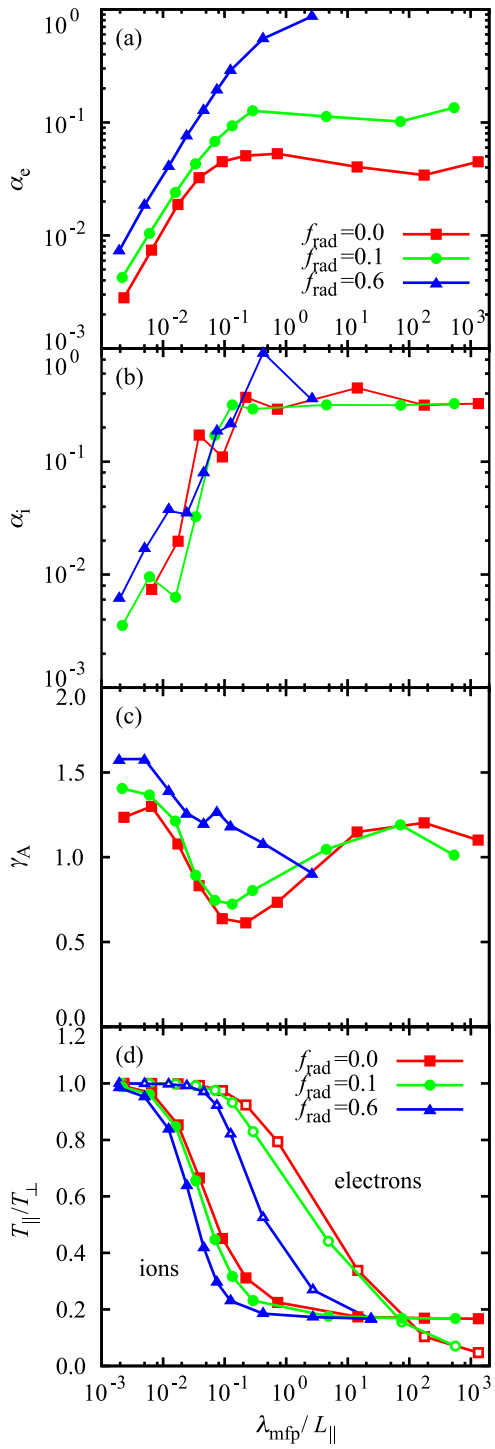

Fig. 4 Dependence of kinetic factors on the normalized MFP $\lambda_{mfp}/L_\parallel$: (a) Electron heat flux limiting factor α_e, (b) ion heat flux limiting factor α_i, (c) adiabatic index γ_A, and (d) temperature asymmetry $T_\parallel/T_\perp$. All values measured at equilibrium in range $s/L_\parallel$ = [0.27 : 0.36] with only hot particle source present. Electron and ion temperature asymmetries are marked with hollow and filled symbols, respectively.

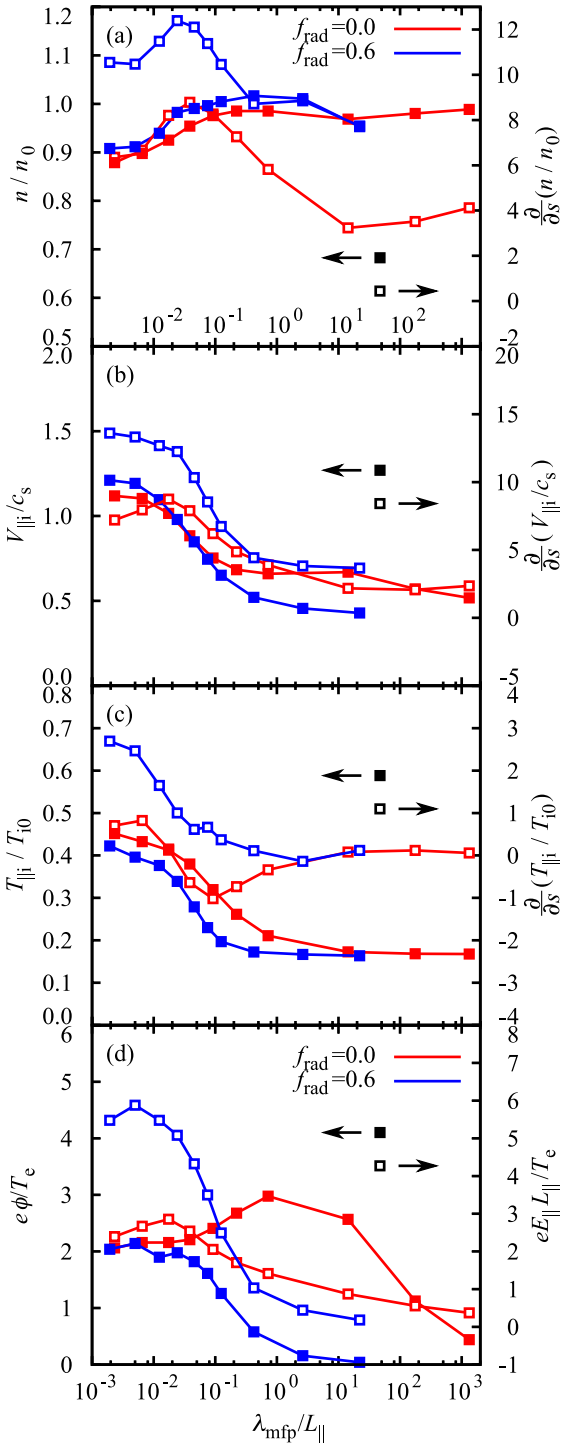

Fig. 5 Dependence of normalized SOL properties on the normalized MFP $\lambda_{mfp}/L_\parallel$: (a) ion density and gradient, (b) Mach number and gradient, (c) ion parallel temperature and gradient, and (d) plasma potential and electric field. Gradients are parallel to magnetic field. All values measured at equilibrium in range $s/L_\parallel$ = [0.27 : 0.36] with only hot particle source present. Values are marked with solid boxes and labeled on the left axis. Gradients are marked with hollow boxes and labeled on the right axis.

tions. One can see that when the density gradient shown in Fig. 5 (a) peaks, the parallel temperature gradient shown in Fig. 5 (c) becomes negative at the same time, permitting the adiabatic index to become less than unity. The drop in ion parallel temperature gradient corresponds to the electric field shown in Fig. 5 (d) falling to zero in the intermediate region, i.e. the plasma changes from a conduction-limited regime to a sheath-limited regime.

Figure 4 (d) shows that over the weakly collisional regime $10^{-2} < \lambda_{\rm mfp}/L_{\parallel} < 1$, the ions shift quickly from being isotropic to the parallel temperature being equal to 1/6 of the perpendicular temperature. When the source ions are cold, the anisotropy in the collisionless limit is $T_{\parallel}/T_{\perp} = 1/3$ because the parallel heat flux is three times higher than the perpendicular heat flux [28]. However, when the ion source is the same temperature as the electron source and the adiabatic index is $\gamma_{\rm A} = 3$, then the ion sound speed doubles. This increases the parallel transport by a factor of two and changes the anisotropy from 1/3 to 1/6. Unlike the ions, the electrons are fully isotropic in the weakly collisional regime and instead become anisotropic over the range $1 < \lambda_{\rm mfp}/L_{\parallel} < 10^2$. The plot indicates that the electrons become even more anisotropic than the ions in the collisionless limit. As the radiation rate increases, the MFP range over which only the ions are anisotropic becomes one order of magnitude instead of two.

The transition from conduction- to sheath-limited plasma is apparent in Fig. 5 (a) in the weakly collisional regime; at $\lambda_{\rm mfp}/L_{\parallel} = 1$ the density becomes unity and there is a large drop in the density gradient. This effect is mitigated by high radiation levels, which maintain the large gradient even in a collisionless plasma so as to keep the density low in the radiation/recycling region. The transition from conduction- to sheath-limited plasma also reduces the ion flow velocity, parallel temperature, and electric field. Both the ion flow velocity and its gradient shown in Fig. 5 (b) decrease by roughly a factor of two when changing from a collisional to a collisionless plasma. Similarly, the ion parallel temperature shown in Fig. 5 (c) decreases by a factor of two, but its gradient decreases precipitously. The reduction in parallel temperature is greater near the source than the divertor, leading to a negative ion temperature gradient. This leads to the aforementioned case of the adiabatic index becoming less than unity. The potential and electric field decrease gradually, with a change of one order of magnitude covering a MFP range of six orders of magnitude, as shown in Fig. 5 (d). However, the presence of radiation causes the transition to shorten to a MFP range of only two orders of magnitude.

All the electron and ion EDFs shown in Fig. 6 exhibit a bulk population and a high-energy tail. The vertical axis is normalized such that the total ion number is unity, $\int_0^1 {\rm d}x \int_{-\infty}^{\infty} {\rm d}v^3 f_{\rm i}(x) = 1$. The horizontal axis is normalized to the source temperature $T_{\rm e0}$ in plots (a) and (c), so the high-energy tails coincide; to the electron parallel temperature $T_{\parallel,{\rm e}}$ in the intermediate region in plot (b); and to the ion sound speed $c_{\rm s}$ in plot (d). The ion distributions are centered on the flow velocity $f_{\rm i}(\tilde{v}_{\parallel})$. Table 2 tabulates the properties of the bulk and tail when fitted to Maxwellian distributions. One can see that the tail temperature, T^t_{σ}, is always near the source temperature, which is unity because of normalization. In a collisionless plasma, the electron distribution has a bulk population of low-energy electrons that are trapped in the SOL and only occasionally get enough energy through collisions to escape. This bulk population should take the form of a cutoff Maxwellian, as can be seen when $\lambda_{\rm mfp}/L_{\parallel} = 20$, $f_{\rm rad} = 0$ in Fig. 6 (a), or even more clearly in Fig. 6 (b). As the plasma becomes more collisional, the trapped population diffuses in velocity space more rapidly, causing the bulk to tend towards a complete Maxwellian distribution, as in the cases with $\lambda_{\rm mfp}/L_{\parallel} = 0.2$. Radiation has the effect of reducing the temperature of the bulk population, but does not affect the tail until after it has passed through the sampling region. Since all distributions in Fig. 6 (b) have a similar magnitude and slope near zero velocity, we can see that the high-energy tail makes a very small contribution to the overall density or plasma temperature. However, because the bulk electron distribution is highly symmetric, the tail is the dominant source of electron heat flux. This shows that the electron heat flux is more dependent on the source temperature than the local temperature, i.e. the core determines the heat flux in the SOL more than the SOL does.

Like the electron distribution, the ion distribution has a low-energy bulk and a high-energy tail population, although the ion distribution is shifted by the fluid velocity. The bulk population is not due to trapping, as is the case with electrons. The source distribution is Maxwellian, but slow diffusion in velocity space steepens the slope at the fluid velocity. Figure 6 (d) shows that the width of the peak

Table 2 Properties of the electron and ion parallel energy distributions shown in Fig. 9 for case with only hot particle source present.

$\lambda_{\rm mfp}$	$f_{\rm rad}$		$n^t_{\rm e}/n^b_{\rm e}$	$T^b_{\rm e}$	$T^t_{\rm e}$
0.2	0.0		0.11/5.7	0.29	0.83
0.2	0.6		0.075/5.8	0.20	0.94
20	0.0		0.075/6.6	0.17	0.90
20	0.6		0.088/5.9	0.016	0.82
$\lambda_{\rm mfp}$	$f_{\rm rad}$	$V_{\parallel,{\rm i}}$	$n^t_{\rm i}/n^b_{\rm i}$	$T^b_{\rm i}$	$T^t_{\rm i}$
0.2	0.0	1.8×10^{-2}	1.0/5.6	0.30	0.69
0.2	0.6	2.0×10^{-2}	0.59/5.7	0.27	0.72
20	0.0	1.3×10^{-2}	1.3/3.4	9.9×10^{-3}	0.70
20	0.6	1.1×10^{-2}	1.6/3.3	7.0×10^{-3}	0.68

Note: MFP $\lambda_{\rm mfp}$ is normalized to connection length $L_{\parallel}$, ion fluid velocity $V_{\parallel,{\rm i}}$ is normalized to source thermal velocity $(T_{\rm i0}/m_{\rm i})^{1/2}$, densities n_{σ} are normalized to make the total ion number unity, and bulk and tail temperatures T^b_{σ}, T^t_{σ} are normalized to source temperature $T_{\sigma 0}$.

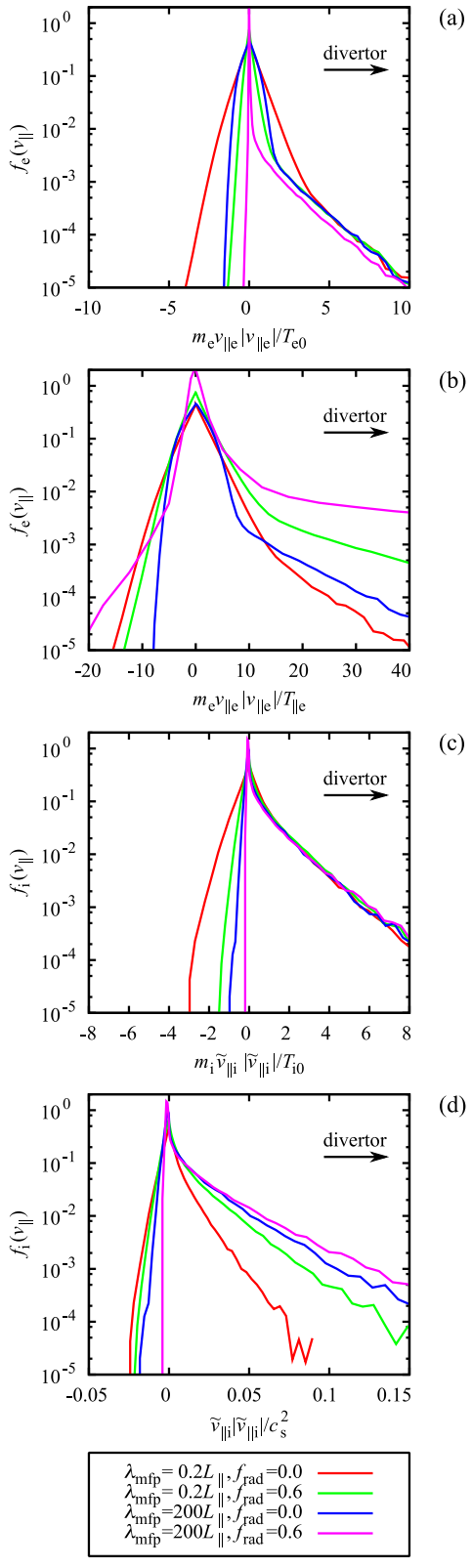

Fig. 6 Electron parallel energy distribution $f_e(v_\parallel)$ with horizontal axis normalized to the (a) source temperature and (b) the local temperature in the intermediate region. Ion distribution $f_i(\tilde{v}_\parallel)$ normalized to (a) source temperature and (b) local parallel ion sound speed in the intermediate region. Positive and negative horizontal axes indicate motion towards and away from divertor, respectively. Hot particle source only.

is related to the MFP for both electrons and ions, but only electrons show a response to the radiation, since ions are not reflected from the sheath.

4.2 Modification of kinetic factors with Langevin heat bath

Testing was performed for the same parameters as in the previous section, but with the addition of Langevin heating. The Langevin heat bath was set to have the same temperature as the hot particle source $T_{L0} = T_{e0} = T_{i0}$ and a relaxation rate of $\nu = 10^{-3}\omega_{pe}$. Figures 7, 8, and 9 show the resulting KF, plasma properties, and EDFs, mirroring the cases without Langevin heating in Figs. 4, 5, and 6.

Activating the Langevin heat bath has a significant effect on all the KF except for the electron heat flux limiting factor α_e, which is shown in Fig. 7 (a). The plot of α_e appears similar to the previous case, although a small anomaly appears at $\lambda_{mfp}/L_\parallel \sim 3$ in the radiationless case because all the gradients reverse in the intermediate region. As the radiation grows from $f_{rad} = 0.0$ to $f_{rad} = 0.6$, the collisionless limit of α_e grows from 0.08 to 0.7. The ion heat flux limiting factor shown in Fig. 7 (b) also has similarities to the reference case. However, the low radiation case of α_i exhibits a strong anomaly between $\lambda_{mfp}/L_\parallel \sim 0.3$ and 3, which causes it to become negative. In the collisionless limit, $\alpha_i \to 0.02$ without radiation, but appears to approach 0.01 when $f_{rad} = 0.6$. In the collisionless regime, Langevin heating strengthens the fluctuations in the intermediate region. In the low radiation cases, fluctuations begin to appear when $\lambda_{mfp}/L_\parallel > 300$, but in the high radiation case, they start as low as $\lambda_{mfp}/L_\parallel > 15$.

The adiabatic index is found to be near unity in the collisional regime. However, in the collisionless case, the gradients lie very close to zero, which makes the adiabatic index γ_A poorly defined. This is indicated in Fig. 7 (c) by the lack of points for the low radiation cases above $\lambda_{mfp}/L_\parallel = 0.1$ and the high radiation case above 3. In the weakly colliisonal regime, high radiation can cause the gradients to point towards the source region. This produces a very large negative value $\gamma_A \sim -4$.

In the collisional case, both the ions and electrons are isotropic, but the ion parallel temperature drops to 1/3 of the perpendicular temperature when the plasma becomes collisionless. As explained for the previous case, since the ion heat flux follows the expression $q_\parallel = 3q_\perp$ [28], the parallel heat is transported away three times faster than the perpendicular heat with a corresponding drop in the parallel temperature. However, since the trapped electrons pass through the Langevin heat bath many times, they tend to remain isotropic.

Figure 8 shows that when Langevin heating is added, the ion density becomes roughly 2/3 as large, but the density gradient becomes much smaller in the weakly collisional and collisionless regimes. In fact, the density gradient may even go to zero. The ion flow velocity is

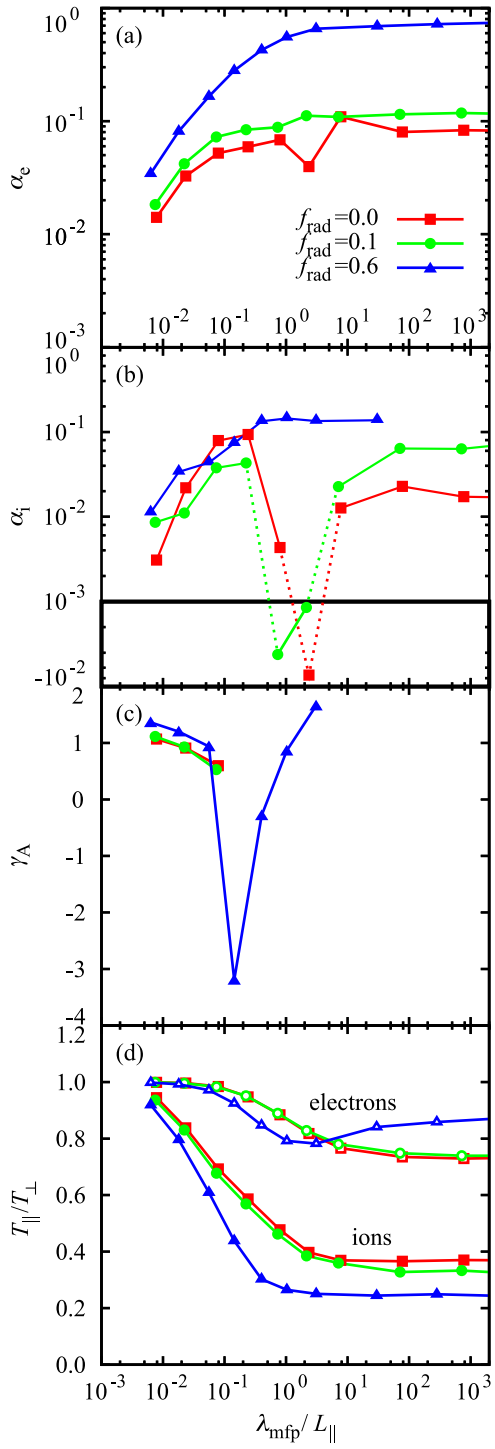

Fig. 7 Dependence of kinetic factors on the normalized MFP: (a) Electron heat flux limiting factor α_e, (b) ion heat flux limiting factor α_i, (c) adiabatic index γ_A, and (d) temperature asymmetry $T_\parallel/T_\perp$. Many points are absent from the γ_A plot because it becomes poorly-defined. All values measured at equilibrium in range $s/L_\parallel$ = [0.27 : 0.36] with Langevin heating present. Electron and ion temperature asymmetries are marked with hollow and filled symbols, respectively.

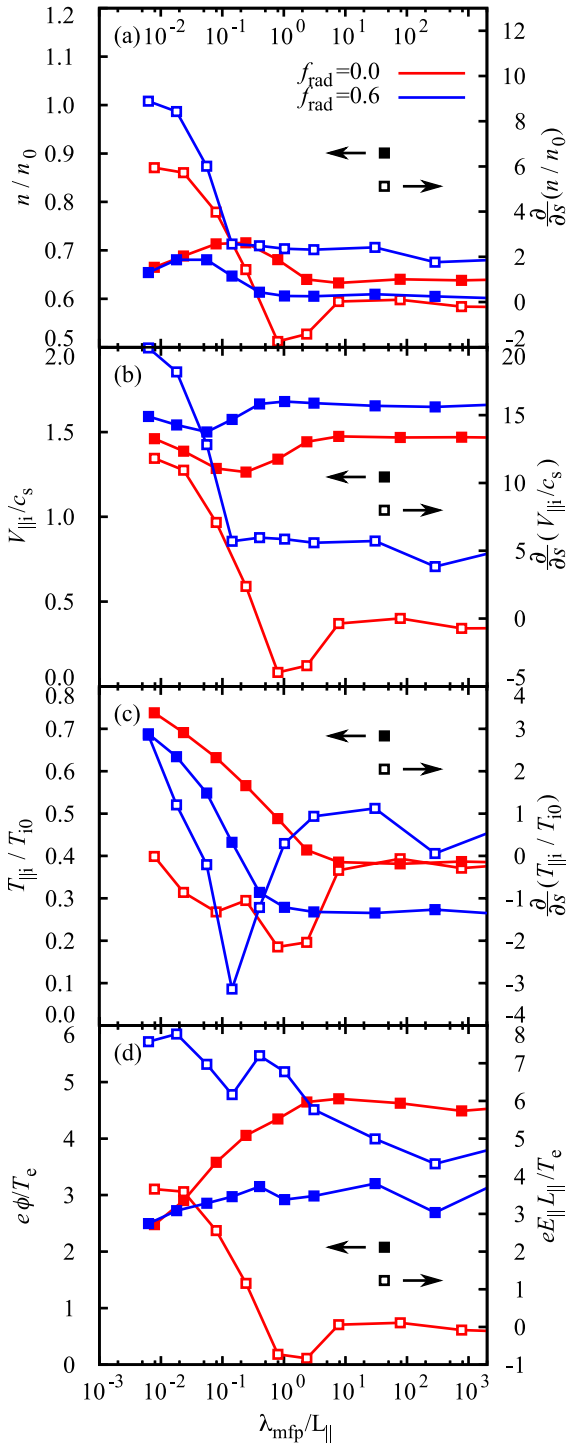

Fig. 8 Dependence of normalized SOL properties on the normalized MFP $\lambda_{mfp}/L_\parallel$: (a) ion density and density gradient, (b) Mach number and gradient, (c) ion parallel temperature and gradient, and (d) plasma potential and electric field. Gradients are parallel to magnetic field. All values measured at equilibrium in range $s/L_\parallel$ = [0.27 : 0.36] with Langevin heating present. Values are marked with solid boxes and labeled on the left axis. Gradients are marked with hollow boxes and labeled on the right axis.

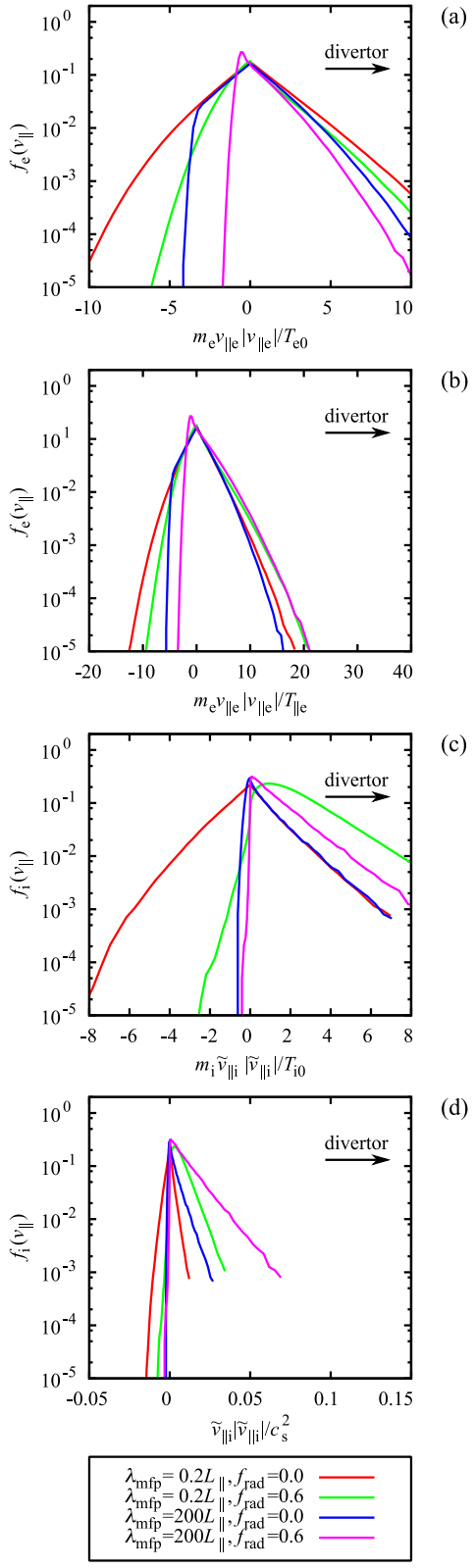

Fig. 9 Electron parallel energy distribution $f_e(v_\parallel)$ with horizontal axis normalized to (a) source and (b) local temperature. Ion distribution $f_i(\tilde{v}_\parallel)$ normalized to (a) source temperature and (b) parallel ion sound speed. Positive and negative horizontal axes indicate motion towards and away from divertor, respectively. Langevin heating present.

Table 3 Properties of the electron and ion parallel energy distributions shown in Fig. 9 for case with Langevin heating present.

λ_{mfp}	f_{rad}		n_e^b	T_e^b
0.2	0.0		4.044	0.921
0.2	0.6		3.234	0.603
20	0.0		3.854	0.882
20	0.6		3.265	0.713
λ_{mfp}	f_{rad}	$V_{\parallel,i}$	n_i^b	T_i^b
0.2	0.0	3.16×10^{-2}	3.7	0.38
0.2	0.6	3.92×10^{-2}	5.7	0.64
20	0.0	3.46×10^{-2}	7.7	0.84
20	0.6	3.88×10^{-2}	8.0	0.78

Note: Same normalizations as Table 2.

roughly constant for all values of the MFP, about 50% faster than the collisionless case when there is no heating, as shown in Fig. 8 (b). When the ions change from collisional and isotropic to collisionless and nonisotropic, there is a range of MFP under which the temperature gradient points towards the source, rather than the divertor, as is the case with both plasma species without Langevin heating. The normalized potential in the intermediate region becomes very large, about a factor of two greater in the collisional regime and a factor of ten greater in the collisionless regime compared to the previous case, as shown in Fig. 8 (d). However, the electric field is almost exactly two times greater than the previous case.

The EDFs for the Langevin heating case are shown in Fig. 9 and the fitted values are recorded in Table 3. Tables 2 and 3 show that the bulk temperatures are generally larger with Langevin heating such that, in most cases, they are very near the source temperature. Comparing Figs. 6 (a) and 9 (a), one can see that Langevin heating eliminates the high-energy tail in the electron EDF. The majority of ions travel at the flow velocity and all ions moving faster than the flow velocity have a Maxwellian distribution with the same temperature as the source, which is shown in Figs. 9 (c) and (d). Unlike the case without heating, there can be a small non-stationary fluctuation in the plasma potential outside the source region that causes ion trapping, resulting in a small population of nearly stationary ions. This population is not shown in Figs. 9 (c) and (d) because it was manually removed for clarity.

One would expect that, due to the tendency of a plasma to approach a Maxwellian distribution in the presence of Langevin heating, the effects of collisionality would be much reduced. Indeed, by comparing Fig. 9 (a) with Fig. 6 (a), one sees that changing the MFP affects the electron distribution much less when Langevin heating is present. However, this is not the case for the ion distribution. One can see in Figs. 6 (c) that without Langevin heating, ions are completely unaffected by electron radiative

cooling. However, Fig. 9 (c) shows that the combination of heating and radiation increases the number of high-energy ions.

5. Summary

We described the fluid model and explained why fluid codes cannot self-consistently solve for the energy distribution function in the scrape-off layer. Closure parameters and boundary conditions at the sheath entrance, so-called kinetic factors, must be provided using theory or fully kinetic simulations. Particle-in-cell codes model the Lorentz force from first principles, so they are useful for exploring the response of kinetic factors to various forcings. We presented results from the PIC code PARASOL-1D for four KF over a wide range of collisionalities, from collisional to collisionless, and explained their behavior using the electron and ion energy distribution functions.

PARASOL-1D shows that the conductive heat flux is accurately described by the Spitzer-Härm expression in the collisional limit and asymptotes to a constant value in the collisionless limit. When the plasma is weakly collisional, such that the plasma is neither conduction- nor sheath-limited, the kinetic factors exhibit many unique characteristics: the heat flux limiting factors α_e and α_i change from MFP proportionality to a constant value; the adiabatic index becomes less than unity because the temperature gradient reverses; and the ions become anisotropic while the electrons remain isotropic. The electron EDFs are Maxwellian in the collisional regime, but in the weakly collisional regime, they form a high-energy tail. As the plasma becomes collisionless, the bulk Maxwellian cut-off velocity due to the sheath potential becomes more clearly defined. The ion EDFs are shifted-Maxwellian distributions with the bulk traveling at the flow velocity and a thermal population traveling faster than the flow velocity.

We investigated the response of the KF to different configurations of energy sources and sinks. Electron radiation energy loss increases the heat flux limiting factors and adiabatic index, while reducing the MFP at which particles become anisotropic, more so for the electrons. The radiation reduces the temperature of the bulk electron distribution, without much affecting the ions. Langevin heating does not have much of an effect on the electron heat flux limiting factor, but it makes both the ion heat flux limiting factor more erratic and the adiabatic index poorly defined. It also prevents the electrons from deviating significantly from an isotropic distribution. Heating thermalizes the electron energy distribution function, but does not affect the ions.

These results should be useful for updating fluid codes, but a more rigorous theory of the weakly collisional regime should be developed to better explain these phenomena. We intend to present an analytic calculation of the heat flux using a simple model of the electron EDF in a forthcoming paper.

Acknowledgments

We would like to thank Mr. M. Hosokawa for his collaboration with regards to the computation and Prof. Andrei Smolyakov for his helpful advice. This work is partially supported by a JSPS Grant-in-Aid for Scientific Research (B) 19360415 and by the collaboration program of RIAM, Kyushu University.

[1] A. Loarte *et al.*, Nucl. Fusion **47**, S203 (2007).
[2] R. Goldston, Phys. Plasmas **17**, 012503 (2010).
[3] L. Tonks and I. Langmuir, Phys. Rev. **34**, 876 (1929).
[4] S.A. Self and H.N. Ewald, Phys. Fluids **9**, 2486 (1966).
[5] G.A. Emmert *et al.*, Phys. Fluids **23**, 803 (1980).
[6] R.C. Bissell and P.C. Johnson, Phys. Fluids **30**, 779 (1987).
[7] R.C. Bissell, P.C. Johnson and P.C. Stangeby, Phys. Fluids B: Plasma Physics **1**, 1133 (1989).
[8] J.T. Scheuer and G.A. Emmert, Phys. Fluids **31**, 1748 (1988).
[9] M. Keilhacker *et al.*, Nucl. Fusion **31**, 535 (1991).
[10] T. Takizuka *et al.*, J. Nucl. Mater. **128**, 104 (1984).
[11] B. Braams, NET report **68**, EUR–FU–XII–80/87/68 (1987).
[12] T.D. Rognlien *et al.*, J. Nucl. Mater. **196-198**, 347 (1992).
[13] R. Simonini *et al.*, J. Nucl. Mater. **196-198**, 369 (1992).
[14] H. Kawashima *et al.*, Plasma Fusion Res. **1**, 031 (2006).
[15] T. Takizuka, M. Hosokawa and K. Shimizu, J. Nucl. Mater. **313-316**, 1331 (2003).
[16] E. Pohn and M. Shoucri, Comm. Nonlinear Sci. **13**, 183 (2008).
[17] W.M. Stacey, *Fusion Plasma Physics* (Wiley-VCH, Weinheim, 2005).
[18] A. Froese, T. Takizuka and M. Yagi, Contrib. Plasma Phys. **50**, 285 (2010).
[19] D. Tskhakaya *et al.*, J. Nucl. Mater. **390-391**, 335 (2009).
[20] A. Hassanein, I. Konkashbaev and L. Nikandrov, J. Nucl. Mater. **290-293**, 1079 (2001).
[21] A. Ferreira *et al.*, Plasma Phys. Control. Fusion **46**, 669 (2004).
[22] P.C. Stangeby, *Plasma Boundary of Magnetic Fusion Devices* (Taylor & Francis, New York, 2000).
[23] S.I. Braginskii, *Transport Processes in a Plasma* volume 1 (Consultant Bureau, New York, 1965).
[24] W. Fundamenski, Plasma Phys. Control. Fusion **47**, R163 (2005).
[25] L. Spitzer and R. Härm, Phys. Rev. **89**, 977 (1953).
[26] T. Takizuka, M. Hosokawa and K. Shimizu, Trans. Fusion Technol. **39**, 111 (2001).
[27] A. Froese, T. Takizuka and M. Yagi, Plasma Fusion Res. **5**, S1017 (2010).
[28] E. Zawaideh and N.S. Kim, Phys. Fluids **31**, 3280 (1988).
[29] R. Schneider *et al.*, Contrib. Plasma Phys. **46**, 27 (2006).
[30] D. Tskhakaya *et al.*, Contrib. Plasma Phys. **48**, 89 (2008).
[31] M. Day *et al.*, Contrib. Plasma Phys. **36**, 419 (1996).
[32] J. Marki *et al.*, J. Nucl. Mater. **363-365**, 382 (2007).
[33] X. Garbet *et al.*, Nucl. Fusion **50**, 043002 (2010).
[34] D. Tskhakaya *et al.*, Contrib. Plasma Phys. **48**, 121 (2008).
[35] C.K. Birdsall and A.B. Langdon, *Plasma Physics via Computer Simulation* (Taylor & Francis, London, 2005).
[36] R.W. Hockney and J.W. Eastwood, *Computer Simulation Using Particles* (McGraw-Hill, New York, 1988).
[37] J.P. Verboncoeur, Plasma Phys. Control. Fusion **47**, A231 (2005).
[38] T. Takizuka and H. Abe, J. Comput. Phys. **25**, 205 (1977).